SUPPORTING INFORMATION

Self-assembly of biaxial discorectangular lead carbonate nanosheets into stacked ribbons studied by SAXS and tomographic HAADF-STEM tilt series

J. Zhang[a], T. Vad[b], M. Heidelmann[cd], T. E. Weirich[ce] and W. F. C. Sager[ad]*

[a]Institute of Complex Systems, Forschungszentrum Jülich, 52425 Jülich, Germany, [b]Institut für Textiltechnik, [c]Central Facility for Electron Microscopy and [e]Institute for Crystallography, RWTH Aachen University, 52074 Aachen, Germany

*e-mail: w.sager@fz-juelich.de

Present Address: [d]Ernst Ruska-Centre for Microscopy and Spectroscopy with Electrons and Peter Grünberg Institute, Forschungszentrum Jülich, 52425 Jülich, Germany

Outline:

(1) Preparation of stacked ribbon assemblies from nonionic water-in-oil microemulsions including Fig. S1 depicting additional SAXS and DLS measurements.

(2) Form factor for discorectangular platelets and Fig. S2 displaying the schematic drawing of rectangular and discorectangular platelets together with their corresponding calculated scattering curves.

(3) Derivation of the structure factor for zig-zag staggered stacked ribbon assemblies (SRAs).

(4) Approximate error term in the structure factor for normally distributed *a*-dimension.

(5) Average number of nanosheets per SRA stacking unit.

(6) 3D animation of the complete HAADF-STEM tilt series of a horizontal lying SRA and the simulated tilting behaviour for abc and ac stacking (Movies S3–S5).

(7) 3D animation of the complete HAADF-STEM tilt series of a vertical lying SRA and the simulated tilting behaviour for abc and ac stacking (Movies S6–S8).

(8) Author's information.

(1) Preparation of stacked ribbon assemblies from nonionic water-in-oil micro-emulsions

A directed and systematic employment of microemulsions as precipitation or reaction media requires at first a characterisation of the microemulsion system also with respect to the changes occurring due to the addition of the reactants themselves.[1-4] In this work, Igepal CO-520 – a nonionic surfactant of the ethoxylated alkylphenol type (nonylphenol with on average 5 ethylene oxide groups) – has been applied to stabilise the water-in-oil (w/o) microemulsions utilised for the synthesis and self-assembly of the $PbCO_3$ nanosheets. In general, the phase behaviour of a nonionic microemulsion system is, in contrast to ionic microemulsion systems, mainly influenced by temperature (T).[5,6] The reason lies in the strong temperature dependence of the hydration of the ethylene oxide moieties. With increasing temperature the hydrogen bonds between the hydrating water molecules and the ether oxygens break and the hydrophilic moiety becomes less soluble and thus less solvated by water. Addition of salt decreases the solubility of the ethylene oxide groups in the aqueous phase further and causes therewith a (slight) lowering in temperature of the observed phase boundaries.[4,7] Spherical water droplets are normally stable below the upper phase boundary (or solubilisation boundary), above which water is expelled from the microemulsion phase into an excess water phase.[5,8] Upon lowering the temperature, the interactions between the spherical droplets can change from being repulsive to becoming attractive and/or structural changes of the water domains can occur.[9] In the latter case cylindrical droplets form that increase in number and length at lower temperature leading finally to an interconnected network of the water domains.[8,10] The extent to which this happens depends on the types of surfactant and oil used and on the water-to-surfactant ratio (W/S).[6,8]

For the water – Igepal – cyclohexane system, (repelling) spherical water droplets are on the oil-rich side stable over a relatively large range of composition and temperature.[11,12] The

microemulsion system with water as interior aqueous phase has been characterised in detail by small angle X-ray scattering and time-resolved mid-infrared pump-probe spectroscopy.[12] At the small water-to-surfactant ratio W/S = 0.2 (which corresponds to a molar water-to-surfactant ratio w_o = 5 that has been used in Reference 12) the microemulsion consists at 303 K of spherical droplets with a radius of 3.8 nm (with a water pool radius of 1 nm and a polydispersity of 18% (log-normal size distribution)) that behave like hard spheres. The corresponding scattering curve is depicted in Fig. S1B and indicates clearly the spherical nature of the microemulsion droplets. It is measured under the same conditions as the dispersion of the SRAs in reverse micellar solution. The refinement of the SAXS curve has been performed using a model function based on Vrij´s analytical solution for a multi-component system of hard spheres.[13,14] Since the electron densities of water and ethylene glycol as well as of the nonylphenol tail and cyclohexane are similar, the part of the microemulsion droplets that contributes to the scattering is the head group shell and interior water, while the tail is invisible to X-rays. The size of the interior water pool is obtained by subtracting the length of the ethylene oxide chain l_h from the measured radius (*i.e.*, 2.9 nm at W/S = 0.2 and T = 303 K). The chain length l_h has been determined from the intercept of a plot of the measured droplet radius versus w_o (see Fig. 3 in Reference 12). The value of 1.8 nm corresponds to an extended chain (zigzag) configuration with a length of 3.5 Å per monomer, which is expected for short ethylene oxide chains (see also the discussion on the value of the interstitial space Z_t between the sheets in the SRA in the scattering section of the main text). The length of the hydrophobic surfactant tail is retrieved from half of the droplet surface–to–surface distance D_0 ($D_0/2$ = 0.91 nm) that is implemented via the structure factor for hard spheres. The time-resolved infrared experiments have shown that in these microemulsion droplets, still 50% of the solubilised water behaves like water that reorients at the same rate as

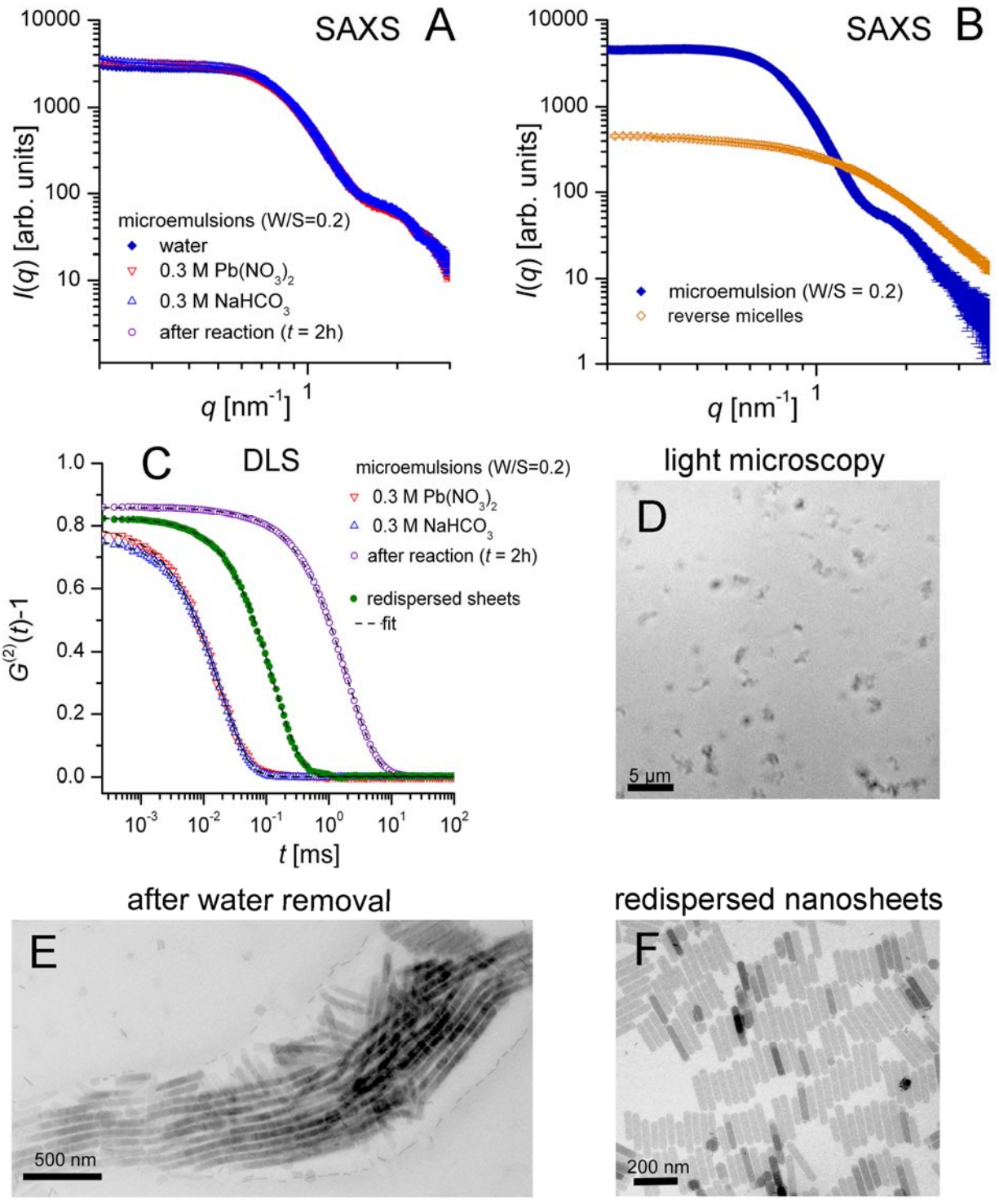

Fig. S1 (A) SAXS curves of nonionic w/o microemulsions for the system aqueous phase – Igepal – cyclohexane at *W*/*S* = 0.2 with water (filled diamonds), 0.3 M $Pb(NO_3)_2$ (open inverse triangles) and 0.3 M $NaHCO_3$ (open upright triangles) as aqueous phase and after a reaction time of 2 h (open circles). (B) SAXS curve of the microemulsion at *W*/*S* = 0.2 with water (filled diamonds) and the reverse micellar solution (open diamonds) at the same surfactant

concentration of 13.6% Igepal in cyclohexane. (C) Intensity autocorrelation functions $G^{(2)}(t)$-1 versus correlation time (t) obtained from dynamic light scattering measurements for the parental microemulsions, the SRA-containing microemulsion and redispersed nanosheets (symbols are the same as in (A)). (D) Optical light microscopy image of the SRA-containing microemulsion. TEM-images of SRAs after water removal (E) and of the redispersed nanosheets (F).

bulk water. The confinement affects thus the reorientation dynamics of only the first hydration layer of the surface bound interior water, which indicates that the ethylene oxide chains do not penetrate into the interior water volume.[12] The salt concentration of 0.3 M used for the synthesis of the nanosheets is clearly below that known to drastically affect the dynamics of water.[15]

Figure S1A shows SAXS curves for the Igepal stabilised microemulsions that contain either water or salt solution (*i.e.*, 0.3 M $Pb(NO_3)_2$ or 0.3 M $NaHCO_3$, respectively, that have been used for the synthesis of the $PbCO_3$ sheets) as aqueous phase. The SAXS data have been measured at the Institute for Complex Systems (ICS-1), Forschungszentrum Jülich, using a Nanostar U SAXS instrument (Bruker AXS, Germany) that is equipped with a microfocus X-ray source and a Våntec 2000 2D gas detector, at a sample-to-detector distance of 1.05 m and a wavelength of 0.15 nm, covering a smaller q-range. The temperature was set to 306 K as for the preparation of the SRAs. The fact that the scattering curves with and without addition of salt fall on top of each other, clearly demonstrates that in this case, the added salt does not lead to changes of the characteristic features of the microemulsion droplets. The scattering curve after mixing both salt-containing microemulsions (*i.e.* 2 h after the reaction has been started) shows still the signature of the microemulsion, indicating that the microemulsion droplets stay always present (independent of the forming particle system). In addition to the scattering curve of the microemulsion at W/S = 0.2 Fig. S1B also displays the scattering intensities of the reverse micellar solution with the same surfactant concentration (13.6% Igepal in cyclohexane), which is already depicted in Fig. 3C. The comparison shows that the scattering contribution of the

microemulsion is about 10 times higher than that of the reverse micelles and shifted to lower q. Comparing Fig. S1B with Fig. 3A illustrates why it was necessary to remove the water from the (reacted and thus SRA-containing) microemulsion by azeotropic distillation. Even the maximum of the first face-to-face interplatelet correlation peak (1st structure factor peak) of the SRAs stays in intensity below the scattering curve of the microemulsion ($I(q)$ < 2000). The scattering contribution of the SRAs would probably have become visible only for q < 0.2 nm^{-1}, whereby all significant features in the scattering curve of the SRAs were covered. Fig. S1E displays a TEM-micrograph of an SRA after water has been removed by azeotropic distillation, showing no significant differences for samples taken before and after water removal. The developed drying procedure for the deposited TEM-grids has been implemented always in the same way and tested for different types of nanoparticles formed.

In order to have an independent way to show the formation of the SRAs within the microemulsion we performed dynamic light scattering (DLS). The DLS experiments were performed with an ALV/CGS-8F S/N 060 laser goniometer system (ALV Laservertriebs-gesellschaft, Germany) with an LV-5000 fast multi-tau digital correlator at a wavelength λ = 632 nm and an angle of 90°. The temperature was set to 306 K. All samples were filtered through a 0.45 μm pore size Nylon filter prior to data collection. The recorded intensity autocorrelation functions[16] for the two parental microemulsions and the SRA-containing microemulsion that has been collected 2 h after starting the reaction by combining the lead and carbonate ion-containing microemulsions are displayed in Fig. S1C. The autocorrelation functions were fitted using a single stretched-exponential decay function to obtain the corresponding relaxation times (τ). Since the two parental microemulsions reveal due to the nanometre size of the containing coated water droplets very fast relaxation times ($\tau = 0.02$ ms), they do not perturb the measured

correlation function of the SRAs. The large value of τ = 2 ms for the SRAs corresponds to micrometre sized objects, and confirms thus that the formation of the self-assembled nanosheet aggregates takes already place within the microemulsion. For comparison the intensity autocorrelation function is also shown for singly dispersed nanosheets (see Fig. S1F) that display with τ = 0.13 ms a 15 times smaller relaxation time. For this sample, the reaction was stopped at 2 h and the microemulsion after dilution by a factor of 3 with cyclohexane placed in an ultrasonic bath for 15 min. In addition, an optical light microscopy image of the SRA-containing microemulsion in the liquid state, taken with an Axioplan 2 microscope (Carl Zeiss, Germany), is shown in Fig. S1D, which also reveals the existence of larger aggregates (SRAs). The reacting microemulsion was in this case placed after 2 h in a rectangular capillary (0.1 x 2 mm^2), which was then sealed on both ends with ultraviolet adhesive glue.

(2) Form factor for discorectangular platelets

The particle form factor amplitude of a discorectangular shaped platelet (DR, see Fig. S2B) is given by

$$F_{\mathrm{DR}}\left(q_x, q_y, q_z\right) = \frac{1}{A_{xy}}\left\{\frac{2J_1\left(q_r R\right)}{q_r R}\pi R^2 \cos\left(q_x a\right) + \frac{\sin\left(q_x a/2\right)}{q_x a/2}\frac{\sin\left(q_y b/2\right)}{q_y b/2} ab\right\}\frac{\sin\left(q_z c/2\right)}{q_z c/2}, \quad \text{(S1)}$$

where $J_1\left(q_r R\right)$ is the first order Bessel-function, $A_{xy} = \pi R^2 + ab$, $q_r = \sqrt{q_x^2 + q_y^2}$, and $R = b/2$. Fig. S2C displays the scattering intensity of a single parallelepiped (PE, see Fig. S2A) calculated with the parameters taken from Table 1 that has been modelled with the DR form factor given in eqn (S1)**,** thus showing that it is within the accessible *q*-range possible to mutually express the scattering behaviour of one of the two form factors by the other. One should, however, keep in mind that for platelets with same thickness *c* and width *b,* the length *a* differs slightly for both

types of platelets at constant particle volume V_p. With $a_{DR} = a_{PE} - \frac{\pi b}{4}$ one obtains for the largest dimension of the DR $l_{DR} = a_{PE} + b\left(1 - \frac{\pi}{4}\right)$, which is larger than the length a_{PE} of the PE. From the fit shown in Fig. S2C we obtain l_{DR} = 127 nm compared to a_{PE} = 118 nm for the parallelepiped. The TEM-images show nanosheets resembling more parallelepipeds with rounded *b*-edges and their length reveals with $\langle a \rangle$ = 121 ± 14 nm a significant size distribution, whereby both lengths (l_{DR} and a_{PE}) fall within the uncertainty of the experimentally determined value.

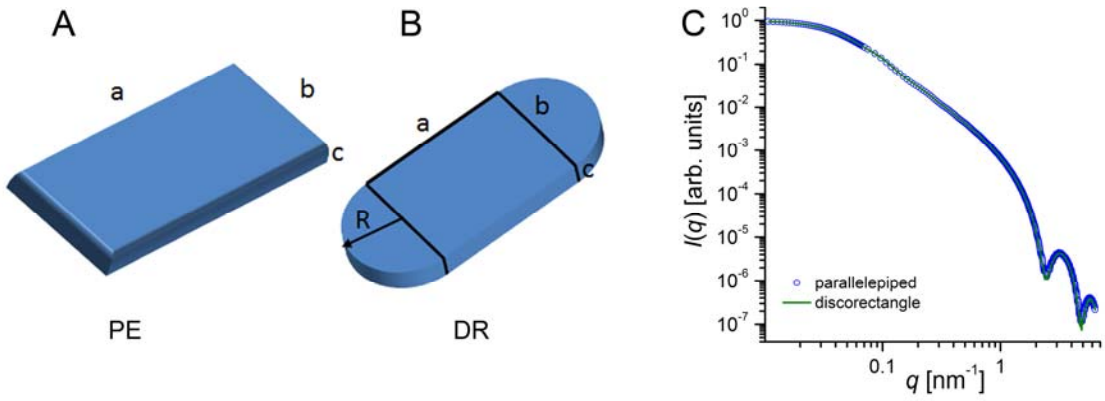

Fig. S2 Parallelepiped with dimensions *a*, *b*, *c* (A), discorectangular platelet (B), calculated scattering intensity of a single parallelepiped modelled with the form factor of a discorectangular platelet (C). The two scattering curves do not differ significantly within the measured *q*-range taking size polydispersity and data accuracy into account. The crystallographic *R*-value for the fit is *R* = 0.0078. The difference becomes more pronounced at higher *q*, when the data become more noisy and the influence of the micellar scattering contribution dominant.

(3) Derivation of the structure factor for zig-zag staggered stacked ribbon assemblies (SRAs).

The general expression for the form factor amplitude of a particle is

$$F(\vec{q}) = \frac{1}{V_\mathrm{p}} \int_{V_\mathrm{p}} \exp\left[-i\vec{q}\vec{r}\right] dV_\mathrm{p}, \quad \text{(S2)}$$

where V_p is the particle volume, $\vec{q}$ is the momentum transfer vector, and $\vec{r}$ is the real space vector defining the particle shape. For a parallelepiped of dimensions *a*, *b*, *c*, the form factor amplitude is given by

$$\begin{aligned} F_0(q_x, q_y, q_z) &= \frac{1}{abc} \int_{-\frac{a}{2}}^{\frac{a}{2}} \int_{-\frac{b}{2}}^{\frac{b}{2}} \int_{-\frac{c}{2}}^{\frac{c}{2}} \exp\left[-i\left(q_x x + q_y y + q_z z\right)\right] dx dy dz \\ &= \frac{\sin(q_x a/2)}{q_x a/2} \frac{\sin(q_y b/2)}{q_y b/2} \frac{\sin(q_z c/2)}{q_z c/2}, \end{aligned} \quad \text{(S3)}$$

where q_x, q_y, q_z are the components of the *q*-vector in Cartesian coordinates (Fig. S2A).

For the form factor with an additional parallelepiped shifted by a vector $\vec{\delta}$ = (δ_x, δ_y, δ_z) relative to the origin of the first particle one obtains

$$F_1(q_x, q_y, q_z) = F_0(q_x, q_y, q_z)\left(1 + \exp\left[-i\omega\left(\vec{\delta}\right)\right]\right), \quad \text{(S4)}$$

whereby the form factor amplitude of the second particle exhibits some phase shift $\omega(\vec{\delta})$ with respect to the first parallelepiped.

The staggered zigzag stacking of the nanosheets induces a 3D *Manhattan* or *Taxicab* geometry [17,18] on the nanosheet system, where the inner product of two vectors is defined as[19]

$$\left\langle \vec{q}, \vec{\delta} \right\rangle = \sum_i \omega_i = \sum_i \varepsilon_i |q_i||\delta_i|, \; i = x, y, z \quad \text{(S5)}$$

and the $\varepsilon_i = \pm 1$ are the signs of the respective components depending on the relative orientation of the vectors $\vec{q}$ and $\vec{\delta}$. Since the phase shift $\omega(\vec{\delta})$ cannot depend on the direction of the real space shift-components δ_i, the 8 possible combinations of the shift components in ±*x*-, ±*y*-, and

$\pm z$-direction are symmetry-equivalent, *i.e.*, $\varepsilon_i = 1\ \forall\ i = x, y, z$ and the phase shift is finally given by

$$\Omega = \omega\left(\vec{\delta}\right) = \left|q_x\delta_x\right| + \left|q_y\delta_y\right| + \left|q_z\delta_z\right|, \quad \text{(S6)}$$

where the shift components in the respective directions are $\delta_x = X_\mathrm{t}$, $\delta_y = Y_\mathrm{t}$, $\delta_z = c + Z_\mathrm{t}$. Hence, one obtains for the scattering amplitude of an SRA consisting of N parallelepipeds

$$F_{\mathrm{SRA}}\left(q_x, q_y, q_z\right) = F_0\left(q_x, q_y, q_z\right)\sum_{k=0}^{N-1}\exp\left[-ik\Omega\right] = F_0\left(q_x, q_y, q_z\right)\sum_{k=0}^{N-1}\cos\left(k\Omega\right) - i\sin\left(k\Omega\right). \quad \text{(S7)}$$

The scattering intensity of an SRA is proportional to the squared modulus of the scattering amplitude

$$I_{\mathrm{SRA}}\left(q_x, q_y, q_z\right) \propto \left|F_{\mathrm{SRA}}\left(q_x, q_y, q_z\right)\right|^2 = F_0^2\left(q_x, q_y, q_z\right)\left\{\left(\sum_{k=0}^{N-1}\cos\left(k\Omega\right)\right)^2 + \left(\sum_{k=0}^{N-1}\sin\left(k\Omega\right)\right)^2\right\}, \quad \text{(S8)}$$

which finally results in

$$I_{\mathrm{SRA}}\left(q_x, q_y, q_z\right) = F_0^2\left(q_x, q_y, q_z\right)V_p^2 S_{\mathrm{SRA}}\left(q_x, q_y, q_z\right), \quad \text{(S9)}$$

where

$$S_{\mathrm{SRA}}\left(q_x, q_y, q_z\right) = N + 2\sum_{k=1}^{N-1}\left(N-k\right)\cos\left(k\Omega\right). \quad \text{(S10)}$$

is the structure factor of the SRA.

(4) Approximate error term in the structure factor for normally distributed *a*-dimension

The unusually large value for the uncertainty in the shift X_t can be explained by the fact that the particle dimensions vary significantly along the *a*-axis. In fact, the TEM analysis shows relative uncertainties of $\sigma_a/a \approx 0.12$, $\sigma_b/b \approx 0.02$ and $\sigma_c/c \approx 0.015$ in the respective dimensions. Since the

relative uncertainty in the *a*-dimension exceeds the other values by almost one order of magnitude, the influence of the less-well defined particle length *a* cannot be neglected.

Assuming that the *a*-dimension is normally distributed around the average value a_0 and a distribution parameter σ_a, the structure factor contains an error-term $f_{\mathrm{err}}(q_x)$, *i.e.*,

$$I_{\mathrm{SRA}}(q) \approx \left\langle F^2(q) V_{\mathrm{p}}^2 \right\rangle_a \left[1 + \frac{2}{N} \sum_{k=1}^{N-1} (N-k) \cos(k\Omega) \exp\left(-\frac{k}{2} \xi^2 \right) f_{\mathrm{err}}(q_x) \right], \quad \text{(S11)}$$

with

$$f_{\mathrm{err}}(q_x) = \frac{\left\langle F(q) V_{\mathrm{p}} \right\rangle_a^2}{\left\langle F^2(q) V_{\mathrm{p}}^2 \right\rangle_a} \approx \frac{\exp\left(-q_x^2 a_0^2 / 12\right)}{\sigma_a^2 / a_0^2 + \exp\left(-q_x^2 \left[a_0^2 + 3\sigma_a^2 \right] / 12\right)} \propto \exp\left(-q_x^2 a_0^2 / 12\right) \quad \text{(S12)}$$

and

$$\left\langle f(a) \right\rangle_a = \frac{1}{\sqrt{2\pi}\sigma_a} \int_{-\infty}^{+\infty} f(a) \exp\left[-\frac{(a-a_0)^2}{2\sigma_a^2} \right] da. \quad \text{(S13)}$$

For a sufficiently large σ_a, the error-term $f_{\mathrm{err}}(q_x)$ can be approximately described by a modified uncertainty factor

$$\sigma_{X\mathrm{t}} \approx \sqrt{a_0^2 / 6 + \sigma_{X\mathrm{t}0}^2}, \quad \text{(S14)}$$

where $\sigma_{X\mathrm{t}0}$ is the pure uncertainty in the *a*-shift (for $\sigma_a \ll a_0$, $f_{\mathrm{err}}(q_x) \approx 1$, which is the case for the shifts along the *b*- and *c*-direction). Using a_0 = 121 nm and $\sigma_{X\mathrm{t}0}$ = 7 nm from the TEM analysis, one obtains $\sigma_{X\mathrm{t}}$ = 49.9 nm which agrees quite well with the refined uncertainty value of $\sigma_{X\mathrm{t}}$ = 48.5 nm.

(5) **Average number of nanosheets per SRA stacking unit**

For the modelling of the SRA scattering contribution, the number N of platelets per stack has been assumed to be constant ($N = N_0$). However, it is possible to discuss the effect of a stack-length distribution on the refined number of platelets N in the model function without loss of generality using the forward scattering intensity $I_{SRA}(0)$, which is given by

$$I_{SRA}(0) = S_0 V_p^2 N_0^2 \equiv S_0 V_p^2 \langle N^2 \rangle \leftrightarrow N_0^2 = \langle N^2 \rangle, \quad \text{(S15)}$$

where $\langle N^2 \rangle$ is the average square of the particles per stack. Assuming that the variation in the stack-length (in z-direction) is described by a length distribution according to Kratky[20]

$$P(l) = \frac{1}{l_{SRA}} \exp\left[-\frac{l}{l_{SRA}} \right], \quad \text{(S16)}$$

where $l_{SRA} = N_p (c_0 + Z_t)$ is the average stack length – an equivalent expression is

$$P(N) = \frac{1}{N_p} \exp\left[-\frac{N}{N_p} \right]. \quad \text{(S17)}$$

Since $P(N = 0)$ corresponds to single particle scattering, it is convenient to define

$$P(\Delta N) = \frac{1}{\Delta N_p} \exp\left[-\frac{\Delta N}{\Delta N_p} \right], \quad \text{(S18)}$$

where $\Delta N = N - 1$, $\Delta N_p = N_p - 1$, and $\langle \Delta N \rangle = 0$ if $N_p = 1$. Thus, the refined number of platelets in the stack N_0 without length distribution is related to the average number N_p by

$$N_0^2 = \langle N^2 \rangle = \langle [1 + \Delta N]^2 \rangle = 1 + 2\int_0^\infty [\Delta N] P(\Delta N) d\Delta N + \int_0^\infty [\Delta N]^2 P(\Delta N) d\Delta N \quad \text{(S19)}$$

which leads to

$$N_0^2 = N_p^2\left[1+\left(1-\frac{1}{N_p}\right)^2\right] \leftrightarrow N_p = \frac{1+\sqrt{2N_0^2-1}}{2} \leq N_0. \quad \text{(S20)}$$

Therefore, the refined value N_0 will be in general larger than the true average value N_p and thus defines an upper limit for the average number of platelets per stack. For the refined value of N_0 = 15 (see Table 1), an average value of N_p = 11 platelets per stack is obtained from eqn (S20)**,** which corresponds to the average value of N_{TEM} = 10 ± 1 derived from the grey-scale analysis of the STEM-micrographs.

(6) 3D animations for the tilting behaviour of a horizontal lying SRA (Movie S3 to S5)

Movie S3

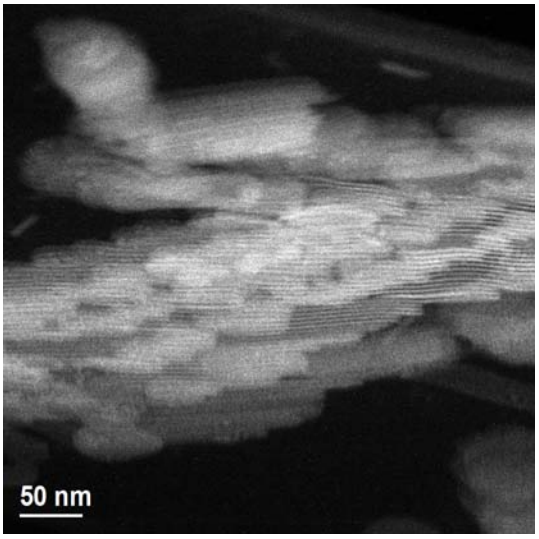

Movie S3 3D animation prepared from the complete tomographic tilt series (horizontal tilt with the tilt axis parallel to the band structure) of HAADF-STEM micrographs (in total 43 images) acquired over an angular range of -66° to +66° with a minimum and maximum tilt angle increment of 1.8° and 4° at high and low angles. The selected image shows the SRAs with the sheets viewed from their long (*a*-*c*) side (reference angle of -90° and experimental tilt angle of the tomography holder of -65°). The movie starts with the lamellar structure and reaches the band structure (*a*-*b* face at a reference angle of 40° and an experimental tilt angle of the holder of 65°), before it turns back.

Movie S4

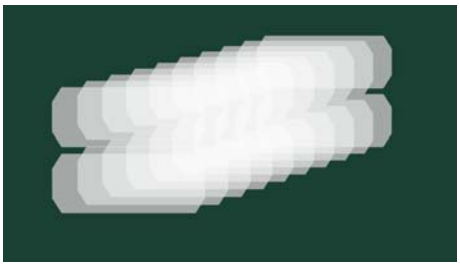

Movie S4 3D animation of the simulated tilting behaviour (horizontal tilt) of two parallel assembled SRA building units consisting of 10 semi-transparent sheets each with abc-stacking (with displacements along the long and short axes of the constituting sheets). The refined parameters from the SAXS measurements, *e.g.*, sheet dimensions and shifts in all three directions, were used for the simulation. The selected snapshot shows the two SRA building units at a tilt angle of 0° revealing a complex interference pattern stemming from the interference between the two neighbouring ribbons. The movie starts at -90° with the lamellar structure and shows the full 360° cycle.

Movie S5

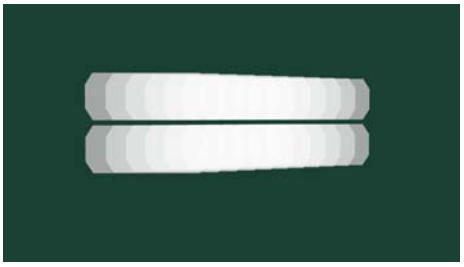

Movie S5 3D animation of the simulated tilting behaviour (horizontal tilt) of two parallel assembled SRA building units consisting of 10 semi-transparent sheets each with ac-stacking (with displacement along the long sheet axis only). The refined parameters from the SAXS measurements, *e.g.*, sheet dimensions and shifts in the *a* and *c* directions, were used for the simulation. The selected snapshot shows the two SRAs building units at a tilt angle of 0° revealing the band structure. The movie starts at -90° with the standing lamellae and shows the full 360° cycle.

(7) 3D animations for the tilting behaviour of a vertical lying SRA (Movie S6 to S8)

Movie S6

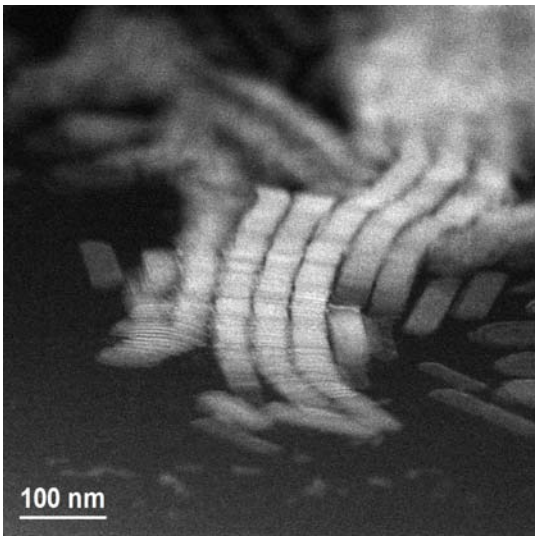

Movie S6 3D animation prepared from the complete tomographic tilt series (vertical tilt with the tilt axis perpendicular to the band structure) of HAADF-STEM micrographs (in total 53 images) acquired over an angular range of -65° to +65° with a step size of 2.5°. The selected image shows the SRAs standing on their short (*b*-*c*) side (reference angle of -90° and experimental tilt angle of the tomography holder of -70°). The movie starts with the lamellar structure. Upon tilting around the short sheet axis, both the sheets and stacks gain in length, revealing a complex interference pattern, before it turns back.

Movie S7

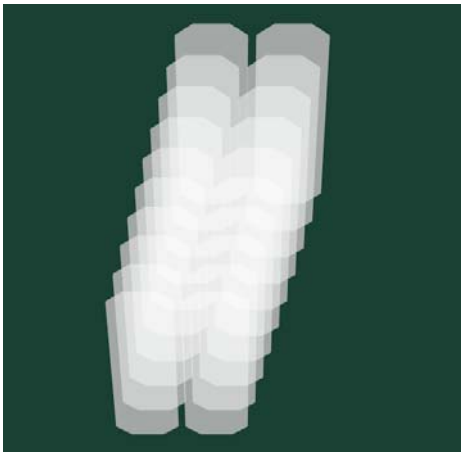

Movie S7 3D animation of the simulated tilting behaviour (vertical tilt) of two parallel assembled SRA building units consisting of 10 semi-transparent sheets each with abc-stacking (with displacements along the long and short axes of the constituting sheets). The refined parameters from the SAXS measurements, *e.g.*, sheet dimensions and shifts in all three directions, were used for the simulation. The selected snapshot shows the two SRAs building units at a tilt angle of -35° revealing a complex interference pattern of the upright standing sheets. The movie starts at 0° with the upright standing SRAs and shows the lamellar structure thus twice by passing through the full 360° cycle.

Movie S8

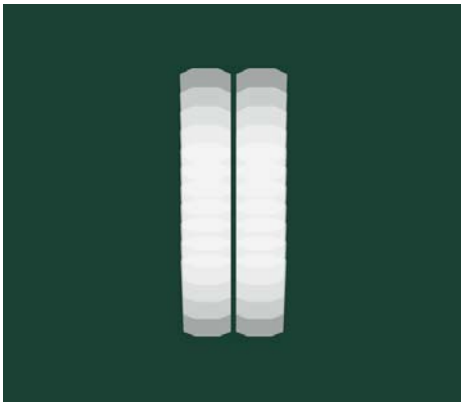

Movie S8 3D animation of the simulated tilting behaviour (vertical tilt) of two parallel assembled SRA building units consisting of 10 semi-transparent sheets each with ac-stacking (with displacement along the long sheet axis only). The refined parameters from the SAXS measurements, *e.g.*, sheet dimensions and shifts in the *a* and *c* directions, were used for the simulation. The selected snapshot shows the two SRAs building units at a tilt angle of -35° revealing the band structure. The movie starts at 0° with the upright standing SRAs and shows the lamellar structure thus twice by passing through the full 360° cycle.

(8) Author's information

Corresponding Author

Dr. Wiebke F. C: Sager
Ernst Ruska-Centre for Microscopy and Spectroscopy with Electrons
and Peter Grünberg Institute,

Forschungszentrum Jülich, 52425 Jülich, Germany

* Contact information for the author to whom correspondence should be addressed: w.sager@fz-juelich.de

References

1. W. F. C. Sager, *Curr. Opin. Colloid Interface Sci.*, 1998, **3**, 276–283.
2. V. Uskokovic and M. Drofenik, *Surf. Rev. Lett.*, 2005, **12**, 239–277.
3. V. Uskokovic and M. Drofenik, *Adv. Colloid Interface Sci.*, 2007, **133**, 23–34.
4. M. Magno, D. G. Angelescu, and C. Stubenrauch, *Colloid Surf. A-Physicochem. Eng. Asp.*, 2009, **348**, 116–123.
5. W. F. C. Sager, in *Nanostructured Soft Matter: Experiments, Theory, Simulation and Perspectives*, ed. A. V. Zvelindovsky, Springer, Doordrecht, 2007, pp 3–44.
6. M. Kahlweit, R. Strey and G. Busse, *J. Phys. Chem.,* 1990, **94**, 3881–3894.
7. M. Kahlweit, R. Strey, P. Firman, D. Haase, J. Jen and R. Schomacker, *Langmuir*, 1988, **4**, 499–511.
8. Strey, R, *Colloid Polym. Sci.*, 1994, **272**, 1005–1019.
9. E. M. Blokhuis and W. F. C. Sager, *J. Chem. Phys.*, 1999**. 110**, 3148–3152.
10. E. M. Blokhuis and W. F. C. Sager, *J. Chem. Phys.*, 2001**. 115**, 1073–1085.
11. S. Lipgens, D. Schubel, L. Schlicht, J. H. Spilgies, G. Ilgenfritz, J. Eastoe and R. K. Heenan, *Langmuir*, 1998, **14**, 1041–1049.
12. T. H. van der Loop, M. R. Panman, S. Lotze, J. Zhang, T. Vad, H. J. Bakker, W. F. C. Sager and S. Woutersen, *J. Chem. Phys.,* 2012, **137**, 044503.
13. A. Vrij, *J. Chem. Phys***.,** 1979, **71**, 3267**–**3270**.**
14. D. Gazzillo and A. Giacometti, *J. Chem. Phys.*, 2000, **113**, 21, 9837–9848.

15. S. Park, D. E. Moilanen and M. D. Fayer, *J. Phys. Chem. B*, 2008, **112**, 5279-5290**.**

16. P. Stepanek, in *Dynamic Light Scattering: The Method and Some Applications*, ed. W. Brown, Clarendon Press, Oxford, 1993, pp 177-241.

17. E. F. Krause, *Taxicab Geometry: An Adventure in Non-Euclidean Geometry.* Dover Publications, New York, 1986.

18. D. J. Schattschneider, *Am. Math. Mon.*, 1984, **91**, 423–428.

19. C. Ekici, I. Kocayusufoglu and Z. Akca, *Turk. J. Math.*, 1998, **22**, 295–307.

20. O. Kratky, *Kolloid Z. Z. Polym.*, 1962, **182**, 7–23.